JPE 16-4-14

http://dx.doi.org/10.6113/JPE.2016.16.4.1375
ISSN(Print): 1598-2092 / ISSN(Online): 2093-4718

# Decoupling of the Secondary Saliencies in Sensorless PMSM Drives using Repetitive Control in the Angle Domain

Chun Wu*, Zhe Chen†, Rong Qi*, and Ralph Kennel**

*School of Automation, Northwestern Polytechnical University, Xi'an, China
†,**Institute for Electrical Drive Systems and Power Electronics, Technical University of Munich, Munich, Germany

## Abstract

To decouple the secondary saliencies in sensorless permanent magnet synchronous machine (PMSM) drives, a repetitive control (RC) in the angle domain is proposed. In this paper, the inductance model of a concentrated windings surface-mounted PMSM (cwSPMSM) with strong secondary saliencies is developed. Due to the secondary saliencies, the estimated position contains harmonic disturbances that are periodic relative to the angular position. Through a transformation from the time domain to the angle domain, these varying frequency disturbances can be treated as constant periodic disturbances. The proposed angle-domain RC is plugged into an existing phase-locked loop (PLL) and utilizes the error of the PLL to generate signals to suppress these periodic disturbances. A stability analysis and parameter design guidelines of the RC are addressed in detail. Finally, the proposed method is carried out on a cwSPMSM drive test-bench. The effectiveness and accuracy are verified by experimental results.

**Key words:** CwSPMSM, Repetitive control, Secondary saliencies, Sensorless control

## I. INTRODUCTION

Sensorless control for ac machines, especially that for permanent magnet synchronous machines (PMSM), has attracted a lot of attention around the world during the past two decades. The elimination of speed/position sensors for ac drive systems can reduce the cost and enhance the reliability of drive systems.

There are two major categories of sensorless control methods: (a) back electromotive-force (EMF) based methods (e.g., sliding mode [1], extended kalman filters [2], adaptive observers [3], etc.) and (b) saliency based methods [4] (normally high-frequency (HF) signal injection is required). Back EMF based sensorless methods are always utilized for machines running in the medium to high speed range. However, these methods fail at low or zero speeds due to the weak signal-to-noise ratio of the back EMF. Fortunately, saliency based methods work well in the low-speed range and at standstill. This is due to the fact that they do not rely upon the back EMF. Instead they extract the angular position by a spatial saliency that is in a fixed relation to the rotor position. These saliencies can be classified into primary and secondary saliencies. The saliency with the maximum magnitude is used for position estimation, and is referred to as the primary saliency [5]. The other saliencies are grouped into secondary saliencies. These may result from magnetic saturation, rotor and stator geometry, manufacturing variations and so on [4], [6]. The existence of multiple saliencies is common in almost all ac machines. If these secondary saliencies are strong and not taken into consideration, they will result in an undesirable estimated position error, which degrades the performance of sensorless control and makes systems unstable [4], [7]. Therefore, this paper focuses exclusively on a method to effectively decouple the secondary saliencies in the sensorless control system.

A decoupling method for secondary saliencies was first proposed by Michael W. Degner. It used an estimated

Manuscript received Dec. 18, 2015; accepted Apr. 2, 2016
Recommended for publication by Associate Editor Jung-Ik Ha.
†Corresponding Author: zhe.chen@tum.de
Tel: +49-89-289-23536, Fax: +49-89-289-28336, Technical University of Munich
*School of Automation, Northwestern Polytechnical University, China
**Institute for Electrical Drive Systems and Power Electronics, Technical University of Munich, Germany

position to build secondary saliency models of an induction motor (IM) and then decoupled them within a phase-locked loop (PLL) [4]. It worked well when the magnitudes of the secondary saliencies were weak [6]. Nonetheless, it was shown to be invalid when the magnitudes of the secondary saliencies were larger than half of the primary saliency [8]. An adaptive controller combined with a neural network was applied to decouple the saturation induced saliencies in interior PMSMs [9]. However, this method required mass commissioning trainings, and the design rules of the neural network were complex. Hence, in the authors' opinions, it is not convenient to carry out in practice. Other similar methods based on a neural network were presented in [10] and faced similar problems. Another attempt through injecting multiple HF signals to extract position information was proposed in [11]. However, the additional HF signals brought a lot more noise and additional power losses to the system. Furthermore, some look-up tables including the HF inductances, which contain several harmonics, were built through the finite element method (FEM) or measurements to decouple the secondary saliencies [12]. Obviously, this method is not easy to extend to other machines due to the different characteristics of the HF inductances.

The methods mentioned above are either difficult to implement or have a high energy consumption. In this paper, a novel repetitive controller (RC) in the angle domain is proposed [13]. The traditional RC method aims to solve the periodic control problem in the time domain. Furthermore, it can be extended to the angle domain [13]. In this paper, the RC concept in the angle domain is applied to decouple the secondary saliencies that are periodic functions of the rotor angle. The RC in the angle domain is easy to realize in a digital controller and is robust to parameter variations when compared with other decoupling methods. The proposed method is applied to a concentrated windings surface-mounted PMSM (cwSPMSM) that shows strong secondary saliencies [8], [11]. The contributions of this paper are as follows:

1) A HF inductance model of a cwSPMSM is developed, which can account for the generation mechanism of the multiple saliencies in sensorless control.
2) A novel angle-domain RC incorporated into a PLL is proposed to decouple the secondary saliencies in the sensorless control of a cwSPMSM.

This paper is structured as follows: Section II analyzes the inductance and develops an inductance model which can demonstrate the characteristics of multiple saliencies for a cwSPMSM. Section III gives a brief introduction to RC and the detailed design principles of the proposed angle-domain RC. Experimental results are shown in section IV. The paper is concluded in section V.

## II. Analyses of Multiple Saliencies of a cwSPMSM

At the frequencies of the injected HF signal, ignoring the effect of the EMF due to the low-speed or zero-speed, the HF model for a PMSM consists only of resistance and inductance terms. With the injected HF signal, the increasing eddy current losses and hysteresis losses are responsible for the increase in the resistance [14]. In [14], [15], the authors point out that the resistances also show a saliency which is called resistive saliency and can be used to estimate the rotor position [16]. In [14], [15] the resistance is measured under different currents and frequencies in distributed windings PMSMs, and it is pointed that the resistance saliency increases with an increase in the frequency of the injected HF signal [16]. However, the inductances show inherent saliencies resulting from different magnetic saturations between direct-axis and the quadrature-axis (*d*- and *q*-axis), which are called inductive saliencies and are strong when compared with resistive saliency [14], [15]. There is no doubt that most methods utilize inductive saliencies to estimate rotor position. In this paper, the inductance model of a cwSPMSM is developed and verified by measurements.

In general, inductances consist of self-inductance and mutual-inductance. Nevertheless, for a cwSPMSM, due to the structure of the concentrated windings, the mutual-inductance between the phases is much smaller than the self-inductance to the magnetic path of the armature reaction [17]-[20]. Furthermore, a cwSPMSM exhibits an intrinsically high slot leakage inductance that is complex to model analytically [20]. Meanwhile, a cwSPMSM shows dedicated spatial saliencies caused by the stator tooth tip saturation due to the rotor zigzag leakage flux [19], which has a reversal property ($L_d > L_q$, $L_d$, $L_q$ are the *d*-axis and *q*-axis inductances, respectively). Hence, a model of a cwSPMSM is different from that of a normal distributed windings SPMSM. In this paper, a simplified inductance model of a cwSPMSM considering only the self-inductance is developed, which is verified in experiments by inductance measurements and HF currents.

### *A. Model of a cwSPMSM Considering Multiple Saliencies*

Ideally, in a machine with sinusoidally distributed windings (sinusoidally magnetic motive force, MMF), the self-inductance and mutual-inductance consist of the dc component and secondary harmonics, shown in Equ (1).

$$\begin{aligned} L_{aa} &= L_0 + L_1\cos(2\theta_e) \\ M_{ab} &= M_0 + M_1\cos\left(2(\theta_e + \pi/6)\right) \end{aligned} \tag{1}$$

where $L_{aa}$ and $M_{ab}$ are the self-inductance of phase *a* and the mutual-inductance between phase *a* and phase *b*, respectively (this notation applies to all of the self and mutual inductances), $L_0$ and $M_0$ are dc components, $L_1$ and $M_1$ are the first harmonics, and $\theta_e$ denotes the electrical position of the *d*-axis advancing to the axis of phase *a*. Furthermore, in distributed-winding machines, $M_0 = -L_0/2$

and $M_1 = -L_1$. However, in concentrated-winding machines, $M_0 \neq -L_0/2$ and $M_1 \neq -L_1$ [21]. Meanwhile, the inductances also have several harmonics [21].

Due to deficiencies in Equ. (1), the inductance model of a cwSPMSM considering harmonics is developed in Equ. (2) [21].

$$\begin{aligned}
L_{aa} &= L_0 + L_1\cos(2\theta_e) + \sum_{i=2}^{\infty} L_i \cos(2i\theta_e + \phi_i) \\
L_{bb} &= L_0 + L_1\cos\big(2(\theta_e - 2\pi/3)\big) \\
&\quad + \sum_{i=2}^{\infty} L_i \cos\big(2i(\theta_e - 2\pi/3) + \phi_i\big) \\
L_{cc} &= L_0 + L_1\cos\big(2(\theta_e + 2\pi/3)\big) \\
&\quad + \sum_{i=2}^{\infty} L_i \cos\big(2i(\theta_e + 2\pi/3) + \phi_i\big) \\
M_{ab} = M_{ba} &= M_0 + M_1\cos\big(2(\theta_e + \pi/6)\big) \\
&\quad + \sum_{i=2}^{\infty} M_i \cos\big(2i(\theta_e + \pi/6) + \phi_i\big) \\
M_{bc} = M_{cb} &= M_0 + M_1\cos\big(2(\theta_e - \pi/2)\big) \\
&\quad + \sum_{i=2}^{\infty} M_i \cos\big(2i(\theta_e - \pi/2) + \phi_i\big) \\
M_{ca} = M_{ac} &= M_0 + M_1\cos\big(2(\theta_e + 5\pi/6)\big) \\
&\quad + \sum_{i=2}^{\infty} M_i \cos\big(2i(\theta_e + 5\pi/6) + \phi_i\big)
\end{aligned} \tag{2}$$

where $\phi_i$ is the phase of the *i*th harmonic. $L_i$ and $M_i$ are the *i*th harmonics of the self-inductance and mutual-inductance, respectively.

To evaluate the inductance model of a cwSPMSM, analytical calculations depending on the detailed design parameters were presented in [20]-[22], and the FEM analysis [15]. However, to implement these methods, the detailed parameters, such as the materials, geometric size, winding factors, etc., must be known exactly. It is impossible to get this information on a commercial machine from the manufacturer. Therefore, measurement methods, such as the ac standstill test [21], [23], or the small-signal perturbation method [14], [15], are preferred by researchers. In the ac standstill test, the neutral line of the stator windings must be available [23]. However, it is not easy to obtain the neutral line in commercial machines. Furthermore if there are no function signal generators or current sensors, etc., the ac standstill test cannot be executed. With respect to the small-signal perturbation method [14], [15], accurate voltage and current sensors are necessary, since the phase and magnitude of the voltages and currents are needed to calculate resistances and inductances. To realize the inductance measurements with a PMSM drive system, a convenient method is adopted here. The authors of this paper use an inverter to generate a HF sin signal, then apply this HF voltage in phases *a* and *b*, and zero voltage in phase *c*. Therefore, the motor stays at standstill. As a result, the phase-to-phase inductance $L_{ab}$ can be measured at one rotor position. Similarly, $L_{bc}$ and $L_{ca}$ can be measured through this method. Then the phase-to-phase inductance is measured at different rotor positions. Fig. 1 shows a diagram of the proposed measurement of the phase-to-phase inductances.

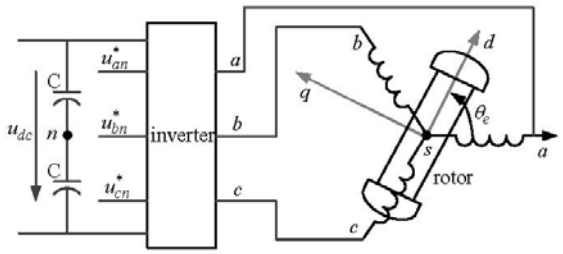


Fig. 1. Diagram of the proposed measurement of phase-to-phase inductance.

Through an inverter, the phase voltages $u_{as}$, $u_{bs}$ and $u_{cs}$ can be obtained as in Equ. (3).

$$\begin{bmatrix} u_{as} \\ u_{bs} \\ u_{cs} \end{bmatrix} = \frac{1}{3}\begin{bmatrix} 2 & -1 & -1 \\ -1 & 2 & -1 \\ -1 & -1 & 2 \end{bmatrix}\begin{bmatrix} u^*_{an} \\ u^*_{bn} \\ u^*_{cn} \end{bmatrix} \tag{3}$$

By setting the inverter reference voltages as $u^*_{an} = U_h\cos(\omega_h t)$, $u^*_{bn} = -U_h\cos(\omega_h t)$, and $u^*_{cn} = 0$, it is possible to obtain, through Equ. (3), $u_{ab} = u_{as} - u_{bs} = 2U_h\cos(\omega_h t)$ (when $i_a \approx -i_b$ and $i_c \approx 0$). Therefore, the phase-to-phase inductances can be calculated from the injected HF voltages and the response HF currents as in Equ. (4).

$$L_{ab} = \frac{\sqrt{\left(|u_{ab}|/|i_a|\right)^2 - 4R_s^2}}{\omega_h} \tag{4}$$

where the $|\ |$ is the amplitude of the sinusoidal component at the angular frequency $\omega_h$, which is obtained by a fast Fourier transform algorithm (FFT) of the phase HF current. $R_s$ is the phase resistances measured by a high-precise LCR meter (Model 878B manufactured by BK PRECISION).

Furthermore, the theoretical inductances between phases *a* and *b* (the other phase is left open) is given by Equ. (5).

$$L_{aa} = L_{aa} + L_{bb} - 2M_{ab} \tag{5}$$

Papers [20], [24] pointed out that the mutual inductances of a concentrated-winding PMSM account for approximately one-tenth of the self-inductance or even less. The major difference between the distributed windings and the concentrated windings is the mutual-inductance. In the design of the concentrated windings, the low mutual-inductance between the phases is required [24]. Therefore, the mutual-inductance is ignored in this analysis. Then Equ. (5) can be revised as Equ. (6).

$$L_{ab} \approx L_{aa} + L_{bb} \tag{6}$$

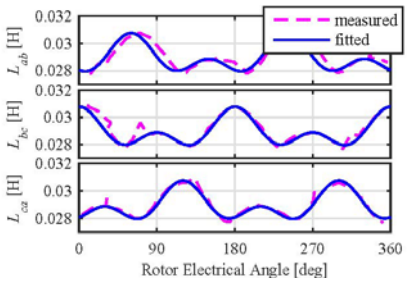


Fig. 2. Measured and fitted phase-to-phase inductances.

To evaluate Equ. (6), the measured and fitted phase-to-phase inductances in relation to the rotor position are shown in Fig. 2.

In Fig. 2, the fitted inductances considering the two main self-inductance harmonics and a dc component are expressed in Equ. (7).

$$\begin{aligned}\hat{L}_{ab} &= 29.1+0.958\cos\left(2\theta_e-2\pi/3\right)+0.759\cos\left(4\theta_e+2\pi/3\right)\\ \hat{L}_{bc} &= 29.1+0.958\cos\left(2\theta_e\right)+0.759\cos\left(4\theta_e\right)\\ \hat{L}_{ca} &= 29.1+0.958\cos\left(2\theta_e+2\pi/3\right)+0.759\cos\left(4\theta_e-2\pi/3\right)\end{aligned} \quad (7)$$

Substituting Equ. (2) into Equ. (6) and comparing the result with Equ. (7) yields $L_0 \approx 14.55$ mH, $L_1 \approx -0.985$ mH and $L_2 \approx -0.759$ mH.

Furthermore, to analyze the influence of inductance harmonics on sensorless control, the position estimation based on Equ. (2) using rotating HF voltage injection is analyzed in the next section.

### *B. Sensorless Control Based on Rotating HF Voltage Injection*

The HF model for a cwSPMSM in the *abc* frame is shown in Equ. (8). (In this case, the stator resistance $R_s$ is less than the reluctance, i.e., $R_s = 2.05\,\Omega \ll \omega_h L_s = 0.0144\times 455\times 2\times\pi \approx 41.15\,\Omega$, where $L_s$ is the stator inductance).

$$\boldsymbol{u}_{abch} = \boldsymbol{L}_{abc}\frac{d\boldsymbol{i}_{abch}}{dt} \quad (8)$$

where $\boldsymbol{u}_{abch}$, $\boldsymbol{i}_{abch}$ and $\boldsymbol{L}_{abc}$ are the stator HF voltage, current and inductance matrix in the *abc* frame, respectively. The subscript $h$ stands for the HF components.

$$\boldsymbol{L}_{abc} = \begin{bmatrix} L_{aa} & 0 & 0\\ 0 & L_{bb} & 0\\ 0 & 0 & L_{cc}\end{bmatrix} \quad (9)$$

Transferring the *abc* frame to the $\alpha\beta$ frame, the HF voltage equation can be expressed as Equ. (10).

$$\boldsymbol{u}_{\alpha\beta h} = \boldsymbol{L}_{\alpha\beta}\frac{d\boldsymbol{i}_{\alpha\beta h}}{dt} \quad (10)$$

where $\boldsymbol{u}_{\alpha\beta h}$, $\boldsymbol{L}_{\alpha\beta}$ and $\boldsymbol{i}_{\alpha\beta h}$ are the voltage, current and inductance in the $\alpha\beta$ frame, respectively.

The structure of a conventional rotating HF voltage injection based sensorless control scheme for PMSMs is shown in Fig. 3, where LPF is the abbreviation for a low-pass filter.

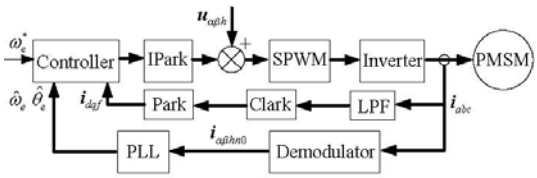


Fig. 3. Structure of the rotating HF voltage injection based sensorless control.

The rotating HF carrier voltage injected into the $\alpha\beta$ frame is expressed as Equ. (11).

$$\boldsymbol{u}_{\alpha\beta h} = U_h\begin{bmatrix}\cos\left(\omega_h t\right)\\ \sin\left(\omega_h t\right)\end{bmatrix} \quad (11)$$

First, transferring Equ. (9) to the $\alpha\beta$ frame and then using Equs. (10) and (11), the general inductance model and the HF response currents for the rotating HF voltage injection from Equ. (11) are derived and classified below in terms of different $i$ indexes. For simplicity, denote $\theta_{ei} = \theta_e + \phi_h/(2i)$ and consider one $i^{th}$ harmonic.

1). For $2i = 3n+1,\ldots$, $n$ is odd.

$$\boldsymbol{L}_{\alpha\beta} = L_0\begin{bmatrix}1 & 0\\ 0 & 1\end{bmatrix} + \frac{L_i}{2}\begin{bmatrix}\cos\left(2i\theta_{ei}\right) & -\sin\left(2i\theta_{ei}\right)\\ -\sin\left(2i\theta_{ei}\right) & -\cos\left(2i\theta_{ei}\right)\end{bmatrix} \quad (12)$$

To express the HF currents clearly, complex coordinates are used, by setting the $\alpha$-axis as the real-axis, and the $\beta$-axis as the imaginary-axis. The HF currents response to the HF voltages are shown in Equ. (13).

$$\boldsymbol{i}_{\alpha\beta h} = I_{cp}e^{j(\omega_h t-\pi/2)} + I_{cn}e^{j(-2i\theta_{ei}-\omega_h t-\pi/2)} \quad (13)$$

2). For $2i = 3n+2,\ldots$, $n$ is even.

$$\boldsymbol{L}_{\alpha\beta} = L_0\begin{bmatrix}1 & 0\\ 0 & 1\end{bmatrix} + \frac{L_i}{2}\begin{bmatrix}\cos\left(2i\theta_{ei}\right) & \sin\left(2i\theta_{ei}\right)\\ \sin\left(2i\theta_{ei}\right) & -\cos\left(2i\theta_{ei}\right)\end{bmatrix} \quad (14)$$

$$\boldsymbol{i}_{\alpha\beta h} = I_{cp}e^{j(\omega_h t-\pi/2)} + I_{cn}e^{j(2i\theta_{ei}-\omega_h t-\pi/2)} \quad (15)$$

3). For $2i = 3n+3,\ldots$, $n$ is odd.

$$\boldsymbol{L}_{\alpha\beta} = \left(L_0+L_i\right)\begin{bmatrix}1 & 0\\ 0 & 1\end{bmatrix} \quad (16)$$

$$\boldsymbol{i}_{\alpha\beta h} = \frac{U_h}{\omega_h\left(L_0+L_i\cos\left(2i\theta_{ei}\right)\right)}e^{j(\omega_h t-\pi/2)} \quad (17)$$

where the magnitudes of the positive-sequence and negative-sequence HF currents are $I_{cp} = U_h L_0/\omega_h\left(L_0^2 - L_i^2/4\right)$ and $I_{cn} = U_h L_i/\left(2\omega_h\left(L_0^2 - L_i^2/4\right)\right)$, respectively. The subscripts *cp* and *cn* represent the positive-sequence and negative-sequence HF current respectively.

Second, when considering two harmonics, such as those in Equ. (7) where $2i = 2$ and $2i = 4$, by using Equs. (13) and (15), the HF currents are expressed in Equ. (18).

$$\boldsymbol{i}_{\alpha\beta h} = I_{cp}e^{j(\omega_h t-\pi/2)} + \boldsymbol{i}_{\alpha\beta hn} \quad (18)$$

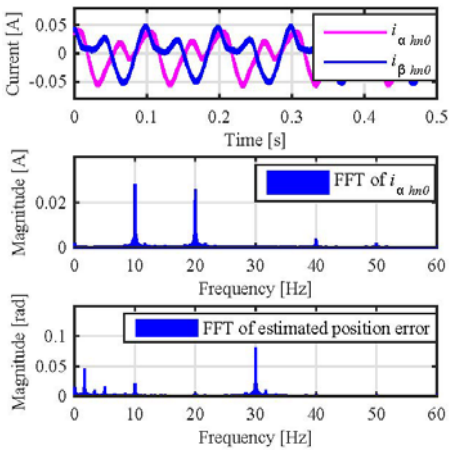


Fig. 4. Pure-NSC in $\alpha\beta$ frame (top), FFT of $\alpha$ -axis pure-NSC (middle), and FFT of the estimation position error (bottom).

where:

$$\boldsymbol{i}_{\alpha\beta hn} = I_{cn1} e^{j(-\omega_h t + 2\theta_{e1} - \pi/2)} + I_{cn2} e^{j(-\omega_h t - 4\theta_{e2} - \pi/2)}$$

$$I_{cp} = \frac{U_h L_0}{\omega_h \left( L_0^2 - \frac{L_1^2}{4} - \frac{L_2^2}{4} - \frac{L_1 L_2 \cos(6\theta_e + 4\phi_2)}{2} \right)}$$

$$I_{cn1} = \frac{U_h L_1 / 2}{\omega_h \left( L_0^2 - \frac{L_1^2}{4} - \frac{L_2^2}{4} - \frac{L_1 L_2 \cos(6\theta_e + 4\phi_2)}{2} \right)}$$

$$I_{cn2} = \frac{U_h L_2 / 2}{\omega_h \left( L_0^2 - \frac{L_1^2}{4} - \frac{L_2^2}{4} - \frac{L_1 L_2 \cos(6\theta_e + 4\phi_2)}{2} \right)}$$

where $I_{cn1}$ and $I_{cn2}$ represent the magnitudes of the 1st and 2nd negative-sequence HF currents (NSC), resulting from the 1st and 2nd inductance harmonics. $I_{cp}$ stands for the positive-sequence HF current. From Equ. (18), the NSC $\boldsymbol{i}_{\alpha\beta h}$ contains position information. It is convenient to utilize some processes and a PLL to extract the rotor position [4]. The principle diagram is shown in Fig. 3.

To verify the HF current derived above, a rotating HF voltage signal is injected into the $\alpha\beta$ frame. The frequency and magnitude of this HF voltage are 455 Hz and 20 V, respectively, and the electrical fundamental frequency is $f_e = 5$ Hz. The pure negative sequence HF currents (pure-NSC: $\boldsymbol{i}_{\alpha\beta hn0} = \boldsymbol{i}_{\alpha\beta hn} e^{j\omega_h t}$ ) in the $\alpha\beta$ frame and the FFT of the $\alpha$ -axis pure-NSC are depicted in Fig. 4.

Fig. 4 shows that the two main harmonic HF currents are also the 2nd-order and 4th-order, which is in accordance with the inductance harmonics and the current derivations in Equ. (18).

The error signal $i_{err}$ is obtained by taking the vector cross-product between the measured pure-NSC $\boldsymbol{i}_{\alpha\beta hn0}$ and the estimated 2nd components from the pure-NSC currents $e^{j(2\hat{\theta}_e - \pi/2)}$, expressed in Equ. (19).

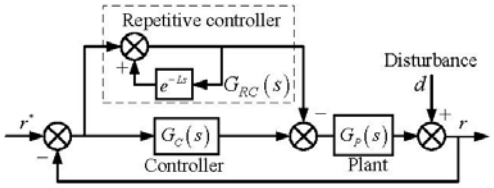


Fig. 5. Structure of plug-in RC.

$$\begin{aligned} i_{err} &= \left| e^{j(2\hat{\theta}_e - \pi/2)} \times \boldsymbol{i}_{\alpha\beta hn0} \right| \\ &= I_{cn1} \sin\left(2\left(\theta_e - \hat{\theta}_e\right)\right) + d_{n2} \end{aligned} \tag{19}$$

where $d_{n2} = I_{cn2} \sin\left(-4\theta_e - 2\hat{\theta}_e - \phi_2\right)$. When $\hat{\theta}_e$ tracks $\theta_e$, the estimated position contains a 6th-order harmonic in one electrical period. From the FFT of the estimated position error ( $\theta_e - \hat{\theta}_e$ ) in Fig. 4, the estimated position contains a 6th-order harmonic ( $5 \times 6 = 30$ Hz). Meanwhile the 8th-order harmonic (40 Hz) is present in the pure-NSC in Fig. 4. However, in the FFT of the estimated position error, the 6th-order harmonic is obvious and the 10th harmonic is tiny, which means that the 8th-order harmonic of the pure-NSC is positive sequence. Hence, these results verify that inductance model Equ. (9) is reasonable.

## III. Repetitive Control in the Angle Domain

The principle of RC originates from the internal model theory [25]. That is, the outputs can track a set of reference inputs without steady-state errors only if the models that have the same internal models of the reference signals are incorporated into the stable closed-loop system. For example, when a system is required to have a zero steady-state error for a step input whose internal model is $1/s$, then $1/s$ should be included in the loop gain. Similarly, if a periodic disturbance is injected into the system, the controller needs to generate the same periodic signal to compensate it for a zero steady-state error [26].

RC is usually implemented as a plug-in module to the original controller, shown in Fig. 5. In presence of a periodic disturbance $d$ whose period is $L$, if the controller $G_C(s)$ and the plant $G_P(s)$ do not contain the internal model of the disturbance, the steady-state error cannot be eliminated due to $d$. According to the internal model theory, the RC, shown as $G_{RC}(s)$ containing the delay function $e^{-Ls}$, which can generate any periodic signal with the period $L$, is inserted into the system in parallel with $G_C(s)$ as a supplement to compensate for $d$ [26].

### *A. Design of RC in the Angle Domain*

In this paper, a modified topology of the plug-in RC, shown in Fig. 6(b), is proposed. This topology advances the

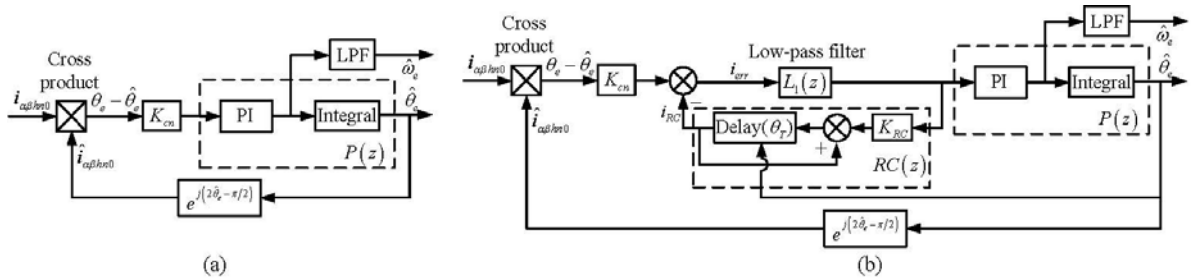


Fig. 6. Structure of the modified PLL with plug-in RC in an angle domain: (a) original PLL, (b) PLL with RC.

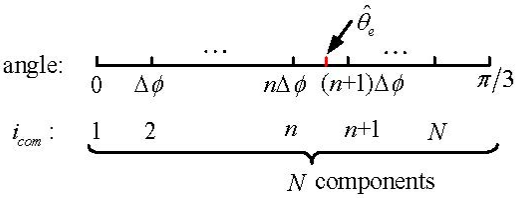


Fig. 7. Realization of RC in angle domain.

output of the RC to the input of the PLL. Because the disturbance $d_{n2}$ is incorporated in the PLL's input, this topology can eliminate disturbances immediately and the disturbances will not affect the other parts of the PLL.

In Fig. 6(b), $L_1$ is a LPF to eliminate the noise of the input of the RC; $K_{RC}$ is the gain of the RC; $P(z)$ is the open loop gain of the original PLL; $K_{cn}$ is equal to $2I_{cn2}$, where $I_{cn2}$ can be obtained from a FFT of the pure-NSC.

The proposed RC being carried out in the angle domain means that the period is not relative to time, but to the angular position $\theta_e$. From Equ. (19), when $\hat{\theta}_e$ tracks $\theta_e$, the term $d_{n2}$ is equal to an angular periodic disturbance, which will induce the output of the PLL ($\hat{\theta}_e$) to track $d_{n2}$. Hence, $\hat{\theta}_e$ contains harmonics due to $d_{n2}$. Unfortunately, the period of $d_{n2}$ is not constant, but varies with the motor speed. Normal RC in the time domain can only handle constant frequency period disturbance compensation. However, from the aspect of the angular position, $d_{n2}$ reappears 6 times in one electrical circle $0 \sim 2\pi$. Independent of the motor speed, the reappearance times in one electrical circle is fixed, which means that $d_{n2}$ is a periodic disturbance relative to $\theta_e$.

For the test cwSPMSM, from Equ. (19), the estimated position contains a 6th-order harmonic angular disturbance in the angle domain. This period in the angle domain is obtained as below.

$$\theta_T = \frac{2\pi}{6} = \frac{\pi}{3} \tag{20}$$

where $\theta_T$ is an angular periodic constant. $i_{err}$ and $\hat{\theta}_e$ are sampled together as inputs to the RC . When $\hat{\theta}_e$ approaches $\theta_e$, the RC generates an output $i_{RC}$ to approximate $d_{n2}$. Then $i_{RC}$ is subtracted from the input of the PLL to compensate $d_{n2}$. Gradually, the term $i_{err}$ tends to zero and $d_{n2}$ will be totally compensated by the RC.

To implement RC in a digital controller, a discrete RC should be designed. The angular period $\pi/3$ is equally divided into $N$ components, shown in Fig. 7, and each component has a length of $\Delta\phi = \pi/(3N)$.

Every sampling instance, if the value of $\hat{\theta}_e$ modulo $\pi/3$ (the whole range 0-2$\pi$ with respect to 0-6$N$) is between $n\Delta\phi$ and $(n+1)\Delta\phi$, then the adjacent upper or lower integer should be chosen. This paper adopts the lower integer, as shown in Equ. (21).

$$i_{RC,k} = i_{com,k-1}[n] \tag{21}$$

where $i_{com,k-1}$ is an array of $N$ lengths at $(k-1)T_s$. $k$ is the sampling instant $kT_s$, and $T_s$ is the sampling time. $i_{RC,k}$ is the output of the RC at $kT_s$. The learning process is expressed in Equ. (22), in which $i_{com,k}[n]$ is updated by $i_{com,k-1}[n]$ and $i_{err,k}$.

$$i_{com,k}[n] = i_{com,k-1}[n] + K_{RC}L_1(i_{err,k}) \tag{22}$$

To describe the proposed RC more clearly, Fig. 8 shows detailed processes at $kT_s$. At every sampling instance, the calculations of the proposed RC consist of a one-order LPF, a mod to determine the location of $\hat{\theta}_e$, and a multiplication and an addition to update the storage array $i_{com}$. A limitation restricts the output of the RC.

### *B. Design Criteria of RC*

In this section, the stability criterion of the PLL with RC is derived and then the design of its parameters is introduced in detail. For simplification, assuming the motor operates at a steady speed $\omega_e$, the analysis can be carried out in the time domain. Therefore, the delay period $\theta_T = \pi/3$ in the angle domain is equal to $T = \pi/(3\omega_e)$ in the time domain.

In Fig. 6(b), the $z$-transfer function between the output $\hat{\theta}_e$ and the input $\theta_e$ of the modified PLL is expressed by

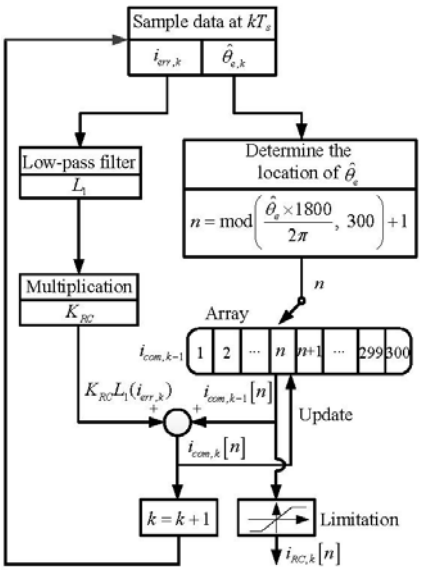

Fig. 8. Flow chart of the calculation of the proposed RC.

Equ. (23).

$$\frac{\hat{\theta}_e(z)}{\theta_e(z)} = \frac{\frac{L_1(z)}{1+L_1(z)RC(z)} \times K_{cn}P(z)}{1+\frac{L_1(z)}{1+L_1(z)RC(z)} \times K_{cn}P(z)} = G_0(z)G_1(z) \quad (23)$$

where $G_0(z) = K_{cn}L_1(z)P(z)/(1+K_{cn}L_1(z)P(z))$ and $G_1(z) = 1/(1+L_1(z)RC(z)/(1+K_{cn}L_1(z)P(z)))$. $RC(z)$ is the $z$-transformer function of the RC, expressed as Equ. (24).

$$RC(z) = \frac{K_{RC}z^{-M}}{1-z^{-M}} \quad (24)$$

where the periodic parameter $M$ is an intermediate integer variable ($M \approx \pi/(3\omega_e T_s)$) that is introduced to analyze the stability.

By substituting Equ. (24) into Equ. (23), the denominator of $G_1(z)$ is denoted by $H(z)$, as shown in Equ. (25).

$$H(z) = z^M - 1 + \frac{K_{RC}L_1(z)}{1+L_1(z)K_{cn}P(z)} \quad (25)$$

From Equ. (23), the stability of the modified PLL can be guaranteed only when all of the poles are located inside the unity circle centered at the origin of the $z$-plane. The requirement for the location of the roots of $G_0(z)$ can be satisfied through proper design of a proportional-integral (PI) controller. The condition for the roots of $G_1(z)$ to be inside the unity circle can be derived using the small gain theorem [25], [26]. By realizing that $z = e^{j\omega T_s}$ and $|z|=1$, this condition can be guaranteed under following requirement [27]:

$$\left|1 - K_{RC}P_1\left(e^{j\omega T_s}\right)\right| < 1 \quad (26)$$

where:

$$P_1\left(e^{j\omega T_s}\right) = \frac{L_1\left(e^{j\omega T_s}\right)}{1+K_{cn}L_1\left(e^{j\omega T_s}\right)P\left(e^{j\omega T_s}\right)} \quad (27)$$

Extending the condition of Equ. (26):

$$\left|1 - K_{RC}A_{P1}(\omega)\cos(\theta_{P1}) - jK_{RC}A_{P1}(\omega)\sin(\theta_{P1})\right| < 1 \quad (28)$$

where $P_1(e^{j\omega T_s}) = A_{P1}(\omega)\theta_{P1}(\omega)$. Squaring both sides of Equ. (28) and rearranging the inequation, it is possible to obtain:

$$K_{RC} < \min\left(\frac{2\cos(\theta_{P1})}{A_{P1}(\omega)}\right) \quad (29)$$

Set $K_{RC} > 0$, then the phase condition of the modified PLL should meet Equ. (30).

$$|\theta_{P1}| < 90^\circ \quad (30)$$

From the analyses above, the complex stability criterion Equ. (26) can be simplified to the choice of $K_{RC}$ and the design of $\theta_{P1}$.

From Equ. (27), the phase of $P_1$ meets the condition $0 < \theta_{P1}(\omega) < 180^\circ$ for all frequencies. Therefore, it is impossible to design such a RC to meet the sufficient criterion in Equ. (26) for all frequencies [27]. Thereby, the main consideration is that the frequency band of interest should satisfy Equ. (26). For a very low frequency band and at a standstill, this RC cannot satisfy the stability criterion. Therefore, it is desirable to stop the RC and use the learned RC which has been trained in stable frequencies (from the experiments, the performance is not as perfect as the one in the stable frequency range).

At a speed of 100 rpm ($f_e = 5$ Hz), the frequency of a disturbance $d_{n2}$ is 30 Hz. A comparison of two bode diagrams, displaying the original PLL and a PLL with RC, is shown in

Fig. 9.

From

Fig. 9, for the PLL with RC, the disturbance suppression is greatly enhanced (the magnitude at 30 Hz is about –263 dB). Meanwhile, the performance of the position tracking stays the same compared with the original PLL in low frequency ranges. Furthermore, when the motor operates at another speed, the bode diagram will be shifted and the specific 6*k*th-order (*k* is a positive integer) harmonics will be suppressed by the RC due to the fixed angular period and the execution in the angle domain. In other words, the PLL with RC behaves like an adaptive notch filter to suppress the disturbance $d_{n2}$. Based on the above analyses, the stability has no relation to *M*, which means that the stability is independent of the motor speed in a desired frequency range. Hence, once the sufficient stability condition in Equ. (26) is satisfied in the frequency band of interest, the stability of the whole system is ensured. The detailed design processes are described below.

*1) Choice of* $K_{RC}$

The choice of $K_{RC}$ will influence the stability of the whole system. Therefore, firstly the selection principle of

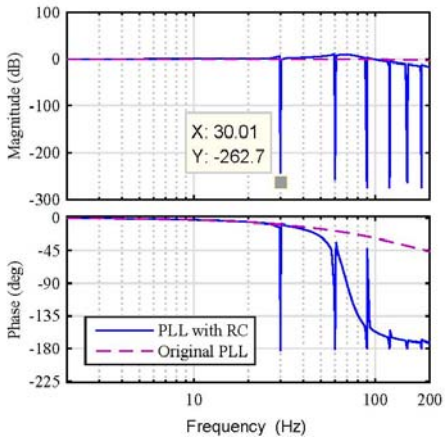


Fig. 9. Bode diagram of the original PLL and the PLL with RC.

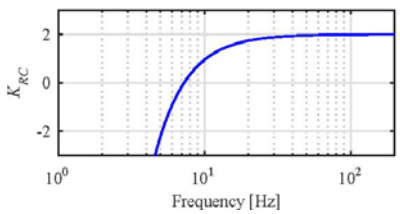


Fig. 10. The change of $K_{RC}$ vs. frequency.

$K_{RC}$ is to ensure that Equ. (29) holds true, and then to obtain fast convergence. A larger $K_{RC}$ will lead to a faster convergence, but worse stability, and vise versa [28]. Hence, the choice of $K_{RC}$ is a tradeoff between stability and the speed of convergence. According to Equ. (29), the maximum $K_{RC}$ varies with frequency, as depicted in

Fig. 10 (the other parameters are given in Section Ⅴ).

Fig. 10 shows that $K_{RC}$ reaches a maximum value of 2 at medium and high frequencies, and decreases sharply at low frequencies. Considering the uncertainties of a system, $K_{RC}$ should be chosen so that it is smaller than the maximum value to ensure system stability.

*2) Design of $L_1$*

$L_1$ is plugged into the RC loop to attenuate noise. However, adding $L_1$ will change the phase and magnitude of $P_1$. Hence, the stability of the modified PLL should be checked first. $P_1$ without $L_1$ is expressed as Equ. (31) (here, the cutoff frequency of $L_1$ is 27 Hz).

$$P_1\left(e^{j\omega T_s}\right)=\frac{1}{1+K_{cn}P\left(e^{j\omega T_s}\right)} \tag{31}$$

A comparison of the phase angle of $P_1$ with and without $L_1$ is shown in Fig. 11.

In Fig. 11, although $L_1$ leads to a decrease in $\theta_{P_1}$, $\theta_{P_1}$

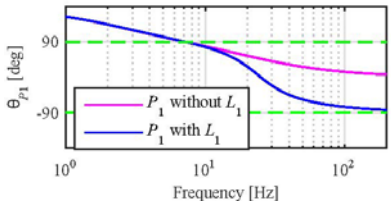


Fig. 11. The phase of $P_1$ with and without $L_1$.

TABLE I
PARAMETERS OF THE CWSPMSM

| Parameter | Value |
|---|---|
| DC link voltage | 582 V |
| Rated power | 2.2 kW |
| Stator resistance | 2.05 Ω |
| Stator inductance | 14.4 mH |
| Pole pairs | 3 |
| Slots | 9 |
| Permanent flux linkage | 0.26 Wb |

still meets the phase condition of Equ. (30). Furthermore, it is apparent from Fig. 11 that the frequency ranges whose phases are between $90^\circ$ and $-90^\circ$ are identical for the original PLL and the PLL with RC. Hence, $L_1$ does not affect the stability of the original PLL. In addition, a high cutoff frequency of $L_1$ introduces a lot of noise to the RC, while a low cutoff frequency will decrease the dynamic response of the PLL. Therefore, a suitable cutoff frequency for $L_1$ should be chosen considering both the anti-noise performance and the dynamic performance of the PLL. A first order LPF is designed using the zero-order hold discretization method, as shown in Equ. (32).

$$y_k = ay_{k-1}+(1-a)x_{k-1} \tag{32}$$

where $a=e^{-2\pi f_{cL1}T_s}$; $f_{cL1}$ denotes the cutoff frequency; and $y_k$ and $x_k$ are the output and input of $L_1$ at $kT_s$.

## IV. EXPERIMENTAL RESULTS

The proposed strategy is applied to a cwSPMSM on an experimental test bench, and the parameters of the cwSPMSM are given in Table 1. A 3 kW induction machine, driven by a LUST (a drive manufacturer) 14 kVA inverter, is used as a load machine. The cwSPMSM is driven by a modified SEW (a drive manufacturer) 5.0 kW inverter which provides full control of the insulated gate bipolar translator (IGBT) gates and has a dead time of 1 $\mu$s. A laboratory built 3.06 GHz real time Pentium computer system is used as a digital controller. The sampling frequency is 16 kHz, while the pulse-width modulation (PWM) frequency is 8 kHz. The rotor position is measured by a 4096-point incremental encoder. The structure of the sensorless control cwSPMSM

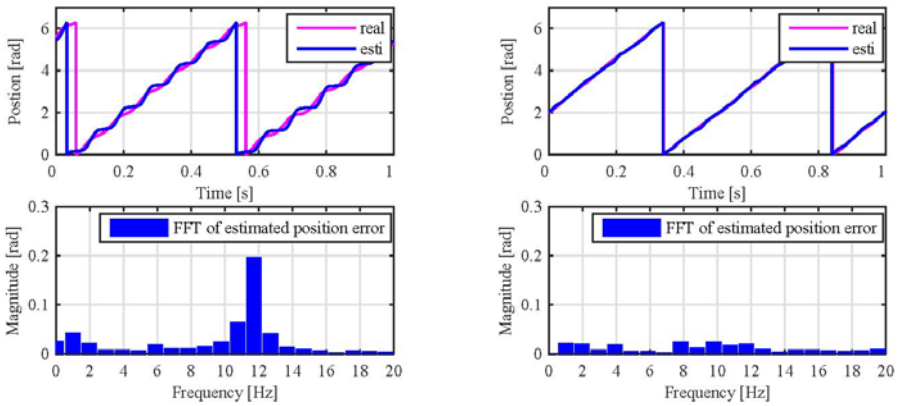


(a) PLL without RC. (b) PLL with RC.

Fig. 12. Comparison of position estimation between PLL without RC and with RC at 40 rpm.

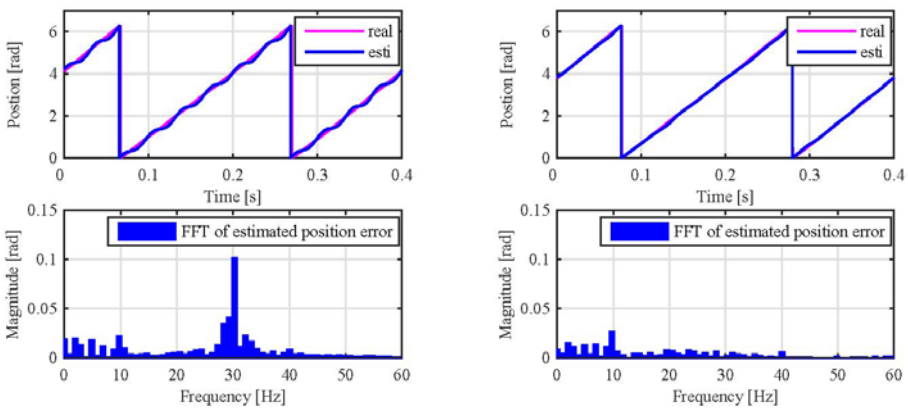


(a) PLL without RC. (b) PLL with RC.

Fig. 13. Comparison of position estimation between PLL without RC and with RC at 100 rpm.

drive system is shown in Fig. 3. The control strategy is vector control realized by sinusoidal PWM (SPWM). The speed and current loops adopt PI controllers.

The frequency and magnitude of the rotating HF voltage are 455 Hz and 10 V, respectively. The parameters of the PLL are: $K_P = 600$, $K_I = 8000$ and $K_{cn} = 0.26$. The RC is designed according to the criteria described in Section Ⅲ. The cutoff frequency of $L_1$ is $f_{cL1} = 27$ Hz. $N = 300$ is selected in the experiment, which means that the phase-interval between two adjacent points is $60^\circ / 300 = 0.2^\circ$. The maximum value of $N$ has the condition that $60^\circ / N \approx 360^\circ / 4096 = 0.088^\circ$. Nevertheless, a large $N$ means a large store memory in the digital controller. In this experiment, $N = 300$ is large and accurate enough to compensate for disturbances. The RC gain $K_{RC}$, according to Equ. (29) and the experimental adjustments, is set to 0.1 in the experiment. The *d*-axis current reference is 3 A (to increase the saliency ratio) and the motor operates under the sensorless speed closed-loop control. With regard to the initial position estimation for the test cwSPMSM, this method is well described in [29].

Fig. 12 shows the position tracking performance of the PLL with and without RC at 40 rpm ( $f_e = 2$ Hz) with half of the rated torque (about 3.6 N.m). Fig. 12 shows that both the real position and estimated position contain a 6th-order harmonic (12 Hz). From the FFT of the estimated position error ( $\theta_e - \hat{\theta}_e$ ) in Fig. 12(a), the magnitude of the 6th-order harmonic is approximately 0.2 rad. After adopting the proposed method shown in Fig. 12(b), the real position and estimated position become much smoother and the magnitude of the 6th-order harmonic is near to 0.

Fig. 13 shows similar results at 100 rpm ( $f_e = 5$ Hz). The 6th-order harmonic (30 Hz) is also suppressed effectively.

Fig. 14 illustrates the convergence of the estimated position error with different values of $K_{RC}$ at 100 rpm without a load (under sensor closed-loop control). It is obvious that a larger $K_{RC}$ results in a faster error convergence, and vice versa. However, when $K_{RC} = 2$, as shown in Fig. 14(c), the RC estimated position error fails to converge which means that a larger $K_{RC}$ induces instability of the original PLL. From Fig. 10, the maximum value of $K_{RC}$ is 2. To ensure the stability margin of the modified PLL, set $K_{RC} = 0.1$ and the theoretical range of stable frequencies observed from Fig. 10

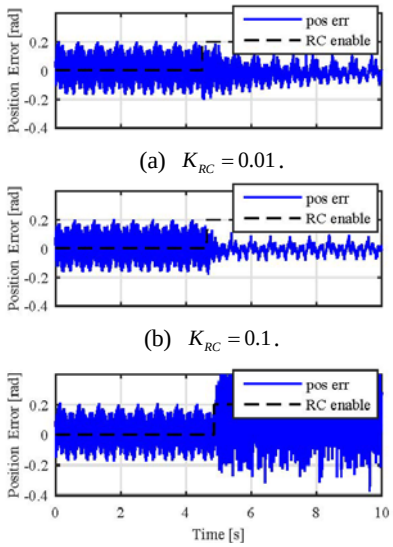


(a) $K_{RC}=0.01$.

(b) $K_{RC}=0.1$.

(c) $K_{RC}=2$.

Fig. 14. Speed of convergence with different $K_{RC}$

is above 7.25 Hz ( $f_e=7.25/6=1.21$ Hz). However, in practice, the stable frequencies start from 9 Hz ( $f_e=9/6=1.5$ Hz). This difference may result from other harmonic components and other uncertainties.

Fig. 15 shows a comparison of the PLL with and without RC under a step change of half of the rated torque at 100 rpm. The original PLL can track the step change. However, due to the high ripple of the estimated position, the estimated speed and current contain large harmonics, as shown in Fig. 15(a). Adopting the PLL with RC, the ripple of the estimated position, the estimated speed and the $q$-axis current are reduced in Fig. 15(b).

The dynamic performance of the step speed command with half of the rated torque is shown in Fig. 16. When the speed command steps from 100 rpm to 200 rpm, using the proposed method, the estimated position, the estimated speed and the $q$-axis current in Fig. 16(b) (PLL with RC) become more accurate than those in Fig. 16(a) (PLL without RC).

Fig. 16 illustrate that the proposed RC in the angle domain can effectively decouple the secondary saliency under different torques and speeds, achieving better dynamic and steady performance than the original PLL.

Through adopting RC into the PLL in the case of a

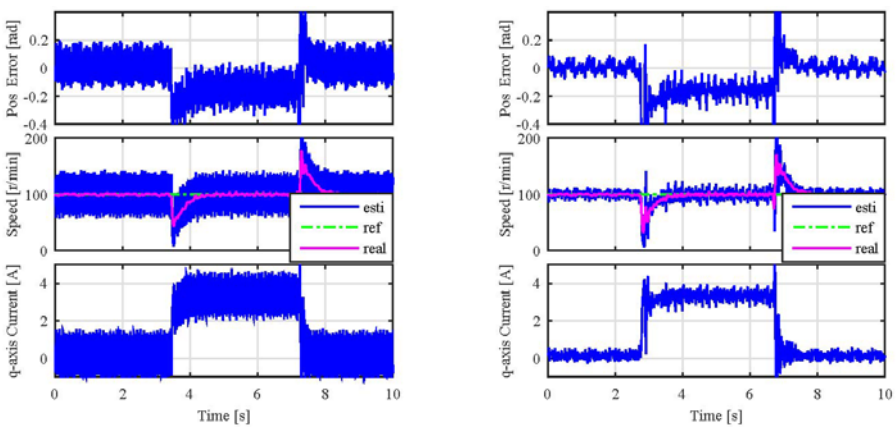


(a) PLL without RC. (b) PLL with RC.

Fig. 15. Comparison of the dynamic performance for a step in the load torque to half rated torque at 100 rpm.

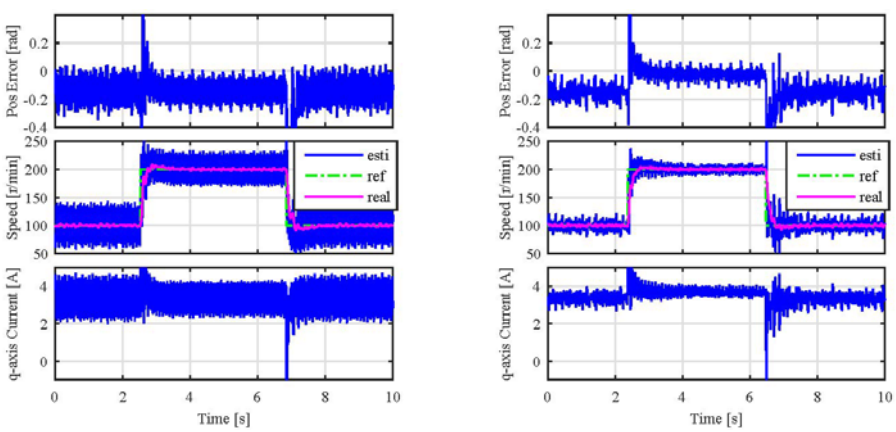


(a) PLL without RC. (b) PLL with RC.

Fig. 16. Comparison of the dynamic performance for a step in the reference speed at half rated torque.

cwSPMSM, it is possible to reduce the ripple of the estimated position, the estimated speed and the motor current, which will improve the dynamic performance to some extent when compared with the PLL without RC. The increase in the gain of the PLL will extend the bandwidth of the PLL, and accelerate the convergence rate of the estimated position and estimated speed. However, a larger gain of the PLL will introduce more noise to the estimated position and estimated speed, and degrade the steady-state performance. Hence, the choice of the gain of the PLL is a compromise between dynamic and steady performances.

## V. CONCLUSION

This paper proposes a novel angle-domain repetitive control (RC) method to decouple the strong secondary saliencies in sensorless PMSM drives. A simplified inductance model considering only the self-inductance is developed for the test cwSPMSM. The strong secondary saliencies can be attributed to the harmonics of the inductance. The estimated position using the HF signal injection based method contains harmonics relative to the angular position due to the secondary saliencies. The stability analysis and parameter choices of the RC are introduced in detail. The proposed RC is parameter independent. Only the frequencies of the secondary saliencies are needed, which are easily obtained by the FFT analysis of the estimated position error. Hence, it is easy to implement in a digital controller and can act as a supplement to the original PLL to suppress harmonic disturbances. The application of this novel decoupling method is applied to a test cwSPMSM. The experimental results validate its effectiveness of decoupling the secondary saliency under different speed and load conditions. The proposed method is valid for other machines with three or more saliencies through RC in parallel mode. Furthermore, this method can be extended to compensate or track periodic disturbances relative to the angular position in other areas.

## ACKNOWLEDGMENT

This research has been supported in part by Deutsche Forschungsgemeinschaft (DFG) KE 817/28-1, and in part by Chinese Scholarship Council.

## REFERENCES

[1] G. Wang, Z. Li, G. Zhang, Y. Yu, and D. Xu, "Quadrature PLL-based high-order sliding-mode observer for IPMSM sensorless control with online MTPA control strategy," *IEEE Trans. Energy Convers.*, Vol. 28, No. 1, pp. 214–224, Mar. 2013.

[2] Z. Peroutka, V. Šmídl, and D. Vošmik, "Challenges and limits of extended Kalman filter based sensorless control of permanent magnet synchronous machine drives," in *13th European Conference on Power Electronics and Applications (EPE)*, pp. 1–11, Sep. 2009.

[3] M. A. Hamida, J. De Leon, A. Glumineau, and R. Boisliveau, "An adaptive interconnected observer for sensorless control of PM synchronous motors with online parameter identification," *IEEE Trans. Ind. Electron.*, Vol. 60, No. 2, pp. 739–748, Feb. 2013.

[4] M. W. Degner and R. D. Lorenz, "Using multiple saliencies for the estimation of flux, position, and velocity in AC machines," *IEEE Trans. Ind. Appl.*, Vol. 34, No. 5, pp. 1097–1104, Sep./Oct. 1998.

[5] D. Raca, M. C. Harke, and R. D. Lorenz, "Robust magnet polarity estimation for initialization of PM synchronous machines with near-zero saliency," *IEEE Trans. Ind. Appl.*, Vol. 44, No. 4, pp. 1199–1209, Jul./Aug. 2008.

[6] N. Teske, G. M. Asher, M. Sumner, and K. J. Bradley, "Suppression of saturation saliency effects for the sensorless position control of induction motor drives under loaded conditions," *IEEE Trans. Ind. Electron.*, Vol. 47, No. 5, pp. 1142–1150, Oct. 2000.

[7] M. W. Degner and F. Briz, "Rotor position method," *IEEE Ind. Electron. Mag.*, Vol. 5, No. 2, pp. 24–36, Jun. 2011.

[8] D. Paulus, P. Landsmann, S. Kuehl, and R. Kennel, "Arbitrary injection for permanent magnet synchronous machines with multiple saliencies," in *IEEE Energy Conversion Congress and Exposition*, pp. 511–517, Sep. 2013.

[9] P. García, S. Member, F. Briz, S. Member, D. Raca, and R. D. Lorenz, "Saliency-tracking-based sensorless control of AC machines using structured neural networks," *IEEE Trans. Ind. Appl.*, Vol. 43, No. 1, pp. 77–86, Jan./Feb. 2007.

[10] T. M. Wolbank and M. K. Metwally, "Speed sensorless flux and position control of induction machines based on pulse injection and multiple saliency extraction," in *34th Annual Conference of IEEE Industrial Electronics (IECON)*, pp. 1403–1408, Nov. 2008.

[11] Z. Chen, J. Gao, F. Wang, Z. Ma, Z. Zhang, and R. Kennel, "Sensorless control for SPMSM with concentrated windings using multisignal injection method," *IEEE Trans. Ind. Electron.*, Vol. 61, No. 12, pp. 6624–6634, Dec. 2014.

[12] M. Seilmeier and B. Piepenbreier, "Sensorless control of PMSM for the whole speed range using two-degree-of-freedom current control and HF test current injection," *IEEE Trans. Power Electron.*, Vol. 30, No. 8, pp. 4394–4403, Aug. 2015.

[13] Z. Chen, C. Wu, R. Qi, G. Luo, and R. Kennel, "Decoupling of secondary saliencies in sensorless AC drives using repetitive control," in *17th European Conference on Power Electronics and Applications (EPE ECCE-Europe)*, pp. 1–10, Sep. 2015.

[14] M. Seilmeier, S. Ebersberger, B. Piepenbreier, and S. Member, "Identification of high frequency resistances and inductances for sensorless control of PMSM," in *IEEE International Symposium on Sensorless Control for Electrical Drives and Predictive Control of Electrical Drives and Power Electronics (SLED/PRECEDE)*, pp. 1–8, Oct. 2013.

[15] L. Alberti, N. Bianchi, and S. Bolognani, "High frequency d-q model of synchronous machines for sensorless control," *IEEE Trans. Ind. Appl.*, Vol. 51, No. 5, pp. 3923–3931, Sep./Oct. 2015.

[16] S. C. Yang and R. D. Lorenz, "Surface permanent magnet synchronous machine position estimation at low speed using Eddy-current-reflected asymmetric resistance," *IEEE Trans. Power Electron.*, Vol. 27, No. 5, pp. 2595–2604, May 2012.

[17] N. Bianchi, S. Bolognani, M. Dai Pré, and G. Grezzani, "Design considerations for fractional-slot winding

configurations of synchronous machines," *IEEE Trans. Ind. Appl.*, Vol. 42, No. 4, pp. 997–1006, Jul./Aug. 2006.
[18] F. Briz, M. W. Degner, P. García, and R. D. Lorenz, "Comparison of saliency-based sensorless control techniques for AC machines," *IEEE Trans. Ind. Appl.*, Vol. 40, No. 4, pp. 1107–1115, Jul./Aug. 2004.
[19] S. C. Yang, T. Suzuki, R. D. Lorenz, and T. M. Jahns, "Surface-permanent-magnet synchronous machine design for saliency-tracking self-sensing position estimation at zero and low speeds," *IEEE Trans. Ind. Appl.*, Vol. 47, No. 5, pp. 2103–2116, Sep./Oct. 2011.
[20] B. Prieto, M. Martínez-iturralde, L. Fontán, and I. Elosegui, "Analytical calculation of the slot leakage inductance in fractional-slot concentrated-winding machines," *IEEE Trans. Ind. Electron.*, Vol. 62, No. 5, pp. 2742–2752, May 2015.
[21] R. Dutta, M. F. Rahman, and L. Chong, "Winding inductances of an interior permanent magnet (IPM) machine with fractional slot concentrated winding," *IEEE Trans. Magn.*, Vol. 48, No. 12, pp. 4842–4849, Dec. 2012.
[22] A. M. El-Refaie, Z. Q. Zhu, T. M. Jahns, and D. Howe, "Winding inductances of fractional slot surface-mounted permanent magnet brushless machines," in *Conference Record - IAS Annual Meeting*, pp. 1–8, 2008.
[23] R. Dutta and M. F. Rahman, "A comparative analysis of two test methods of measuring d - and q -axes inductances of interior permanent-magnet machine," *IEEE Trans. Magn.*, Vol. 42, No. 11, pp. 3712–3718, Nov. 2006.
[24] B. Prieto, M. Martínez-Iturralde, L. Fontán, and I. Elosegui, "Fault-tolerant permanent magnet synchronous machine – phase, pole and slot number selection criterion based on inductance calculation," *IET Electric Power Applications*, Vol. 9, No. 2, pp. 138–149, Feb. 2015.
[25] S. Hara, Y. Yamamoto, T. Omata, and M. Nakano, "Repetitive control system: A new type servo system for periodic exogenous signals.pdf," *IEEE Trans. Autom. Control*, Vol. 33, No. 7, pp. 659–668, Jul. 1988.
[26] P. Mattavelli, L. Tubiana, and M. Zigliotto, "Torque-ripple reduction in PM synchronous motor drives using repetitive current control," *IEEE Trans. Power Electron.*, Vol. 20, No. 6, pp. 1423–1431, Nov. 2005.
[27] X. H. Wu, S. K. Panda, and J. X. Xu, "Design of a plug-in repetitive control scheme for eliminating supply-side current harmonics of three-phase pwm boost rectifiers under generalized supply voltage conditions," *IEEE Trans. Power Electron.*, Vol. 25, No. 7, pp. 1800–1810, Jul. 2010.
[28] T.-Y. Doh and J. R. Ryoo, "Robust Stability Condition and Analysis on steady-state tracking errors of repetitive control systems," *International Journal of Control, Automation, and Systems*, Vol. 6, No. 6, pp. 960–967, Dec. 2008.
[29] Z. Chen, F. Wang, G. Luo, Z. Zhang, and R. Kennel, "Secondary saliency tracking-based sensorless control for concentrated winding SPMSM," *IEEE Trans. Ind. Informat.*, Vol. 12, No. 1, pp. 201–210, Feb. 2016.

**Chun Wu** was born in Hangzhou, China, in 1987. He received his B.S. degree in Electrical Engineering and Automation from the Northwestern Polytechnical University, Xi'an, China, in 2010. He is presently working towards his Ph.D. degree in Electrical Machines and Apparatus in the School of Automation, Northwestern Polytechnical University. His current research interests include the sensorless control of PMSMs, and nonlinear control methods applied in the control of machines.

**Zhe Chen** was born in Huozhou, China, in 1986. He received his B.S. and M.S. degrees in Electronic Engineering and Automation from the Northwestern Polytechnical University, Xian, China, in 2008 and 2011, respectively. Since 2011, he has been working towards his Ph.D. degree in the Institute for Electrical Drive Systems and Power Electronics, Technische Universtaet Muenchen, Munich, Germany. His current research interests include predictive control and sensorless control for power electronics and electric drives, renewable energy systems, and the application of field programmable gate array-based digital controllers.

**Rong Qi** was born in China, in 1962. She received her B.S. and M.S. degrees in Electrical Engineering and her Ph.D. degree in Detection Technique and Automaton Device from the Northwestern Polytechnical University, Xi'an, China, in 1984, 1990, and 2005, respectively. She is presently working as a Professor in the School of Automation, Northwestern Polytechnical University. Her current research interests include electric aircraft, motion control, fault diagnosis and fault tolerant control.

**Ralph Kennel** was born in Kaiserslautern, Germany, in 1955. He received his Diploma and Ph.D. degrees in Electrical Engineering from the University of Kaiserslautern, Kaiserslautern, Germany, in 1979 and 1984, respectively. From 1983 to 1999, he held several positions with Robert BOSCH GmbH, Stuttgart, Germany. Until 1997, he was responsible for the development of servo drives. He was one of the main supporters of the VECON and SERCOS interfaces, two multi-company development projects for microcontrollers and a digital interface especially dedicated to servo drives. Furthermore, he took an active part in the definition and release of new standards with respect to the CE marking for servo drives. From 1997 and 1999, he was responsible for the product development of fractional horsepower motors in automotive applications. His main activity was preparing for the introduction of brushless drive concepts to the automotive industry. From 1994 to 1999, he was appointed as a Visiting Professor at the University of Newcastle-upon-Tyne, Tyne and Wear, U.K. From 1999 to 2008, he was a Professor of Electrical Machines and Drives with Wuppertal University, Wuppertal, Germany. Since 2008, he has been a Professor of Electrical Drive Systems and Power Electronics with the Technische Universtaet Muenchen, Munich, Germany. His current research interests include the sensorless control of ac drives, predictive control of power electronics, and hardware-in-the-loop systems. Dr. Kennel is a Fellow of the IEE and a Chartered Engineer in the U.K. Within the IEEE, he is the Treasurer of the Germany Section, as well as the ECCE Global Partnership Chair of the Power Electronics Society.